Measurement of the interfacial strain energy release rate of adhesively bonded structures with metallic substrates before and after water ageing

Johnatan Leplat[a], Georgios Stamoulis[b], Pierre Bidaud[a], David Thévenet[a]

[a]*ENSTA Bretagne, CNRS UMR 6027, IRDL, 2 rue François Verny, 29200 Brest, France*

[b] *Univ. de Bretagne Occidentale, CNRS UMR 6027, IRDL, rue de Kergoat, 29238 Brest, France*

ABSTRACT

In order to measure the interfacial Strain Energy Release Rate (SERR) of adhesively bonded joints with metallic substrates, an alternative to the Tapered Double Cantilever Beam (TDCB) specimen is used here. In particular, the dimensions of one of the two substrates were reduced to create an Asymmetric Tapered Double Cantilever Beam (ATDCB) specimen. The ATDCB specimen has been introduced in the past by other research teams to study the mode I+II cohesive fracture properties of structural adhesives. It is shown the geometric dissymmetry of the ATDCB specimen affects the crack propagation path towards the interface with the smaller (less stiff) substrate. However, this substrate plasticises during the fracture test; hence, a strategy is also presented to evaluate the amount of potential energy spent for this phenomenon and subtract it from the total potential energy induced in the system during the fracture test. After this operation, the SERR of the adhesive under investigation was calculated by means of the Linear Elastic Fracture Mechanics (LEFM) theory before and after water ageing. The results showed a large decrease of the SERR with the increase of the ageing time.

NOMENCLATURE

$\sigma_{max}^{\square}$	maximum principal stress
σ_{max}^{0}	maximum allowable principal stress
$\sigma_{n}^{\square}$	normal stress
$\sigma_{s}^{\square}, \sigma_{t}^{\square}$	shear stresses
σ_{n}^{0}	ultimate tensile strength
$\sigma_{s}^{0}, \sigma_{t}^{0}$	ultimate shear strengths
$\langle\,\rangle$	Macaulay brackets
D	damage parameter
T_n	normal stress component (traction-separation behaviour)
T_s, T_t	shear stress components (traction-separation behaviour)
δ_n	opening relative displacement in normal direction at nodes
$\delta_{s}^{\square}, \delta_{t}^{\square}$	opening relative displacement in shear directions at nodes
δ_m	effective separation
C	specimen compliance
u	overall opening displacement
F	reaction force along the loading axis
$F_{\exp}$	experimental reaction force
F_{num}	numerical reaction force
G_n	strain energy release rate (mode I)
G_s	strain energy release rate (mode II)
G_t	strain energy release rate (mode III)
G_T	total strain energy release rate
m_1, m_2, m_3	mode ratios
G_n^c (¿ G_I^C)	critical strain energy release rate (mode I)
G_s^c	critical strain energy release rate (mode II)
G_t^c	critical strain energy release rate (mode III)
ν	Poisson ratio
E	Young modulus
σ_y	yield strength

ε_y	yield strain
$\underline{\underline{X}}_i$	kinematic hardening tensor
C_i, γ_i	kinematic hardening parameters
R_i	isotopic hardening variable
b_i, Q_i	isotopic hardening parameters

1. Introduction

Multi-material assemblies are used in many industrial structures including marine energy systems [1–4]. For these types of assemblies, adhesives are very frequently preferred over older techniques like bolting or riveting, which mainly suffer from stress concentrations around the screw holes and localised corrosions [5]. However, the use of adhesives is not widely expanded as they also present serious drawbacks like the dependence of their mechanical behaviour from the temperature or the relative humidity and the absence of non-destructive tests to ensure quality and repeatability during their application. Therefore, the study of the mechanical properties of structural adhesives still remains, until nowadays, an open field of investigation.

The design of adhesively bonded assemblies undergoes two principal phases. The first consists in modelling the stress/strain mechanical behaviour to predict crack initiation; the second one concerns the measurement of the energy required to propagate the crack until total failure of the structure. The former leads to the establishment of a crack initiation criterion and the latter to a crack propagation criterion. These two criteria constitute the necessary and sufficient condition to predict the failure load of an adhesively bonded structure; they were first coupled to one by Leguillon *et al.* [6]. Then this coupled criterion was used to predict the failure load of adhesively bonded joints later on by Carrere *et al.* [7] and gave good results for brittle adhesives, whose fracture behaviour can be adequately described by the small-scale deformation theory. To counteract for structural adhesives presenting important non-linear behaviour (which is the most common case), other approaches like the Cohesive Zone Model (CZM) technique [8] have been implemented in the past. For the current study, only crack propagation is under investigation. According to the Griffith's principle [9], this phenomenon takes place once the potential energy introduced in the system passes a critical value: the critical strain energy release rate or fracture toughness (G_I^C). The stress state at the crack tip can be decomposed into three modes: tension (mode I), in-plane shear (mode II) and anti-plane shear (mode III). In the present research, only modes I and II are of interest.

Crack propagation in adhesively bonded structures has been under investigation since 1970s [10–15]. During all these years, three standards have been established to measure the fracture toughness of structural adhesives under mode I load (G_I^C) [16–18], along with two specimen geometries: the Double Cantilever Beam (DCB) and the Tapered Double Cantilever Beam

(TDCB). For adhesives submitted to mixed-mode I+II load, the Mixed Mode Bending (MMB) device has been frequently used by many research teams, even though it has only been standardized for composite materials [16]. In order to examine the mode II fracture properties of structural adhesives and measure the corresponding fracture toughness (G_{II}^{C}), other standardized tests for composite materials have also been implemented, like the End-Notched Flexure (ENF) [19] and the End-Loaded Split (ELS) tests [20]. All previous tests and methodologies make use of the Linear Elastic Fracture Mechanics (LEFM) principles to calculate G_C and consider that the crack propagation path remains always inside the adhesive layer (cohesive failure). However, it is widely known that, despite all precautions taken during the construction of adhesively bonded joints, failure can also occur at the interface with the substrates (interfacial failure). Interfacial failures occur more frequently when assemblies are exposed to environments of high humidity [21], or if a crack inside the adhesive layer is submitted to an asymmetric stress field [22]. The latter causes the crack propagation path to move towards the more stressed of the two substrates, as it is the case for the MMB test [23].

Based on the previous discussions, it is clear that the hypothesis made in the standards [16–20] for the crack propagation path to be inside the adhesive layer in order to measure G_C, can be irrelevant. Indeed, the SERR at the interface with the substrates can be different to the one of the adhesives itself. However, this is only if the adhesion with the adherents has been well established, and the crack propagation path deviates towards the interface with one of the two substrates due to an adopted loading system. Recently, the authors published a study [24] showing a modification of the TDCB specimen geometry to stabilize crack propagation inside the adhesive layer with thin substrate. It consisted of adding beaks at the surface of the TDCB substrates (similarly to what has been done in [25] for the Arcan test); this permitted to measure the fracture toughness of an epoxy adhesive before and after water ageing for 4, 8 and 12 months. The aim of the present research is to measure the interfacial fracture toughness of unaged and water aged adhesively bonded joints, and compare the results with the ones presented in the previous study [24] (using of course the same epoxy adhesive and the same ageing conditions). This is important since water in adhesively bonded structures mainly attacks the interface with the substrates, as it has also been discussed above. This can only be achieved by choosing an appropriate specimen geometry that drives the crack to propagate at the interface in a stable manner. Therefore, the authors decided to use the Asymmetric Tapered Double Cantilever Beam (ATDCB) specimen, which has already been implemented in the past to measure fracture envelopes of structural adhesives in the mixed mode I+II plane

[26-28]. It should be noted that the Asymmetric Double Cantilever Beam (ADCB) specimen [29-30] would have also been suitable to perform the work presented here. Yet, for reasons of consistency with the previous study, the ATDCB was finally preferred. The difference with the TDCB specimen geometry is the lower stiffness of one of the two substrates due to the reduction of its height. This causes an asymmetric stress field at the crack tip and leads to a deviation of the crack propagation path towards the interface with the smaller substrate (as also discussed above). This phenomenon is coupled to an evolution of the mode ratio along the crack propagation which has been characterized for tests performed by means of the ATDCB specimen geometry [26-28]. Moreover, the smaller substrate may plasticize during the fracture tests. Therefore, the strategy developed to characterize the interfacial fracture toughness need to deal with mixed modes and evaluate accurately the energy spent in the plasticisation of the substrate in order to calculate the energy required to propagate the crack.

In the following sections, first a preliminary study is presented in order to justify the suitability of the ATDCB specimen to examine the interfacial fracture properties of structural adhesives and setup experimental parameters and dimensions. The crack bifurcating to the interface is modelled and calculations of the mode ratio with the crack propagation at the interface by means of different Finite Elements (FE) methods are presented. The ATDCB specimen may be suitable for the measurement of the interfacial fracture toughness in mode I (G_I^C) following a particular geometry fitted to the adhesive used. After taking into account the preliminary results, the article continues by presenting the method of preparation of the ATDCB specimens and the experimental procedure and equipment that were used to perform the tests. Hence, it was possible to measure the SERR at the interface with the substrates of unaged and water aged at 4, 8, 12 and 16 months ATDCB specimens, and compare these results with those identified for the same epoxy adhesive in the previous study [24].

2. Numerical preliminary study

In the ATDCB test case, due to the geometrical dissymmetry of the specimens with regards to the adhesive layer, the crack propagation path deviates toward the interface with the smaller substrate. This is because the smaller substrate stresses more during the fracture test. This dissymmetry also results to the addition of a mode II stress component at the crack tip. The coupling of these two phenomena is in accordance with what has also been observed in works on MMB tests [23]: a crack propagating under mixed mode I+II load leads to a propagation to the interface.

The aim of this preliminary study is to understand the effects of dissymmetry on the deviation of the crack propagation path performing linear FE calculations. In addition, the mode ratio during the ATDCB test has to be close to pure mode I. In order to have a coherent comparison with the values of the G_I^C measured in the previous study of the authors [24]. Since the mode ratio highly depends on the difference of the size between the two substrates, the dimension h_{DCB} of the ATDCB specimens (**Figure 1**) need to be optimized. Finally, some preliminary experimental tests were performed on three ATDCB geometries in order to validate the conclusion we had regarding the numerical work. All these operations are illustrated in the sections 2.1 and 2.2.

2.1. Crack propagation in ATDCB test

Since in the previous study of the authors [24], the TDCB sample was used to examine the mode I fracture properties of the same adhesive under investigation, the analysis of these preliminary results will continue with the ATDCB specimen geometry (**Figure 1**). This type of specimen has already been used in previous studies [26-28] to evaluate G_I^C of structural adhesives, under the hypothesis that the crack propagates cohesively. The ATDCB specimen is the addition of one DCB substrate with one TDCB substrate. All TDCB substrates used here had the same dimensions as those given in previous works [24]. For the DCB substrate, different values for the height h_{DCB} (5, 7.5 and 10 mm) were tested numerically and experimentally.

Figure 2 shows the FE model of TDCB and ATDCB specimens that was developed for the needs of the current study by means of the Abaqus™ software. In these models, only the propagation directions were on the interest. The models were built following plane strain assumption, which permit to accurately describe the crack propagation of adhesive thin joints [31]. So, this model was meshed with fully integrated plane strain elements (CPE4). A mesh size of 0.1x0.1 mm^2 for the adhesive layer gave a converged result. The substrates were imposed tie with the joint. Figure 2 shows the boundaries conditions applied. Nodes in the hole of the upper substrate are driven by a reference point of which displacement in the y axis is imposed and displacement in the x axis is fixed. For the lower substrate, nodes in the hole are driven by a reference point of which displacement in x and y directions were fixed. For both reference points rotational around z axis remained free. For both models, the load was applied under displacement control at the speed of 2 mm/min until the propagation is sufficient to determine the crack direction. The eXtended Finite Element Method (XFEM) was used to

study the propagation of the crack in the adhesive. In the XFEM formulation, degrees of freedom were added in order to pass through problems of singularity and discontinuity like crack propagation [32]. The pre-crack (a_0) was created inside the adhesive layer by an initial XFEM crack set to 70 mm. All materials were considered as linear elastic. For matters of confidentiality the mechanical properties of the metallic material could not be exposed. For the mechanical behaviour of the adhesive some tests on bulk specimen following the ISO 527 standard [33] were performed in tension at the unaged state. These tests allowed identifying an elastic behaviour with a Young modulus of 1.55 GPa and a Poisson ratio of 0.4. These same tests gave a tensile strength of 29 MPa. The specimen thickness of the adhesive t_a was set to 1 mm. The mesh density was refined as shown in Figure 2 in order to reach a convergence of the results in the force-opening curves. For these models, a maximum principal stress criterion was used. According to Abaqus™ documentation, this criterion is defined by:

$$f=\left\{\frac{\langle\sigma_{max}\rangle}{\sigma^{0}_{max}}\right\} \qquad \text{(Eq. 1)}$$

where, σ^{0}_{max} represents the maximum allowable principal stress. The symbol $\langle\rangle$ represents the Macaulay brackets with the usual interpretation (i.e., $\langle\sigma_{max}\rangle=0$ if $\sigma_{max}<0$ and $\langle\sigma_{max}\rangle=\sigma_{max}$ if $\sigma_{max}\geq 0$). The Macaulay brackets were used to signify that a purely compressive stress state does not initiate damage. Damage is assumed to initiate when the maximum principal stress ratio (as defined in the expression above) reaches a value of one.

Again, according to Abaqus™ documentation, the damage evolution law describes the rate at which the cohesive stiffness is degraded once the corresponding initiation criterion is reached. A scalar damage variable D represents the averaged overall damage at the intersection between the crack surfaces and the edges of cracked elements. It initially has a value of 0. D monotonically grows from 0 to 1 upon further loading after the initiation of damage. The normal and shear stress components are affected by the damage according to:

$$t_n=\begin{cases}(1-D)T_n, & T_n\geq 0\\ T_n, & otherwise\end{cases} \qquad \text{(Eq. 2)}$$

$$t_s=(1-D)T_s \qquad \text{(Eq. 3)}$$

$$t_t = (1-D)T_t \quad \text{(Eq. 4)}$$

where T_n, T_s, and T_t were the normal and shear stress components predicted by the elastic traction-separation behaviour for the current separations without damage.

To describe the evolution of damage under a combination of normal and shear separations across the interface, an effective separation was defined as

$$\delta_m = \sqrt{\langle \delta_n \rangle^2 + \delta_s^2 + \delta_t^2} \quad \text{(Eq. 5)}$$

The relative proportions of normal and shear separations at a contact point define the mode ratio. Abaqus™ uses three measurements of mode ratio, two that are based on energies and one that was based on tractions. Denoting by G_n, G_s, and G_t the work done by the tractions and their conjugate separations in the normal, first, and second shear directions respectively, and defining $G_T = G_n + G_s + G_t$, the mode ratio definition based on energies was as follows:

$$m_1 = \frac{G_n}{G_T} \quad \text{(Eq. 6)}$$

$$m_2 = \frac{G_s}{G_T} \quad \text{(Eq. 7)}$$

$$m_3 = \frac{G_t}{G_T} \quad \text{(Eq. 8)}$$

For these models, the choice was made to let Abaqus™ to decide the propagation in regard to the calculated mode ratio. So, a unique value of G_C was applied and equal to the value of the cohesive G_{IC} determine in previous works [24]. All materials data for the XFEM are summarized in Table 1.

Figure 3 illustrates the results for the crack propagation path for the TDCB and ATDCB specimens respectively. As it was expected, the crack direction was towards the interface with the smaller substrate for the ATDCB specimen (**Figure 3**b), compared to the TDCB specimen (**Figure 3**a) where the crack remained at the centre of the adhesive layer.

2.2. Calculation of mode ratio in ATDCB test

In section 2.1, it was shown that, for adhesively bonded joints with substrates fabricated out of the same material, the crack propagation path deviates towards the interface with the smaller substrate. Due to the geometrical asymmetry of the specimen, it can be assumed that the crack tip could not submitted to pure mode I load, as it was the case for the TDCB test. Using an ATDCB specimen, considering the asymmetric stress field at the crack tip a mode ratio I+II was introduced [28], depending on the geometry of the substrates. In order to link the G_C measured during the tests to a failure mode, it was necessary to evaluate the applied mode ratio during the test and throughout the crack propagation. Therefore, FE analyses were performed considering interfacial crack propagation. Mode ratio was calculated using FE models on Abaqus™, by means of the Virtual Crack Closure Technique (VCCT) [34]. The boundary conditions and the mesh used were as the ones presented in Figure 2. For the sake of simplicity, all materials were considered in a linear elastic assumption with the material parameters presented in Table 1. The pre-crack was created at the interface and equal to 70 mm. All other parameters, such as the mesh size, and elements type were the same than the XFEM previously presented. The VCCT was applied at the interface upper interface between the DCB substrate and the joint. The mode ratio for each value of the height h_{DCB} was taken as the value at the initiation of the crack and the minimum value of the mode ratio vs crack length curve. This mode ratio evolved with the compliance function of the crack length. VCCT models were performed for three configurations of h_{DCB} (5 mm, 7.5 mm and 10 mm). The 10 mm height test had a more evolving mode ratio than the 5 mm. The initial mode ratio, for the specimen with a 10 mm DCB substrate, was approximately 91% until a minimum of 86%. When for the 7.5 mm and 5 mm height specimen the mode ratio pass through 90% to 86% and 89 % to 87 % respectively. The thinner DCB substrate seemed to be the best configuration as the mode ratio was more constant, and the propagation should be more stable.

These numerical models were done by elastic material and LEFM assumptions. Nevertheless, with thinner substrates (with low h_{DCB} values) substrate could plasticize. The plastic behaviour of the substrate may modify the mode ratio. At this step of the study, experimental tests were performed to go on the optimization of the sample configuration and the value of h_{DCB}.

3. Experimental Results

3.1. Testing process

The tests were carried out by means of an MTS™ universal electro-mechanic tension-compression machine, under displacement control at 2 mm/min. The specimen was loaded until the crack propagated for 10 mm, then unloaded to zero force. This step is necessary in order to generate a sharp initial pre-crack. Data acquisition was performed by means of two cameras: a first one to measure the opening displacement at the loading axis by means of Digital Image Correlation (DIC) and a second one to measure the crack length (**Figure 4**). A white acrylic paint was applied on the joint to have an easier measurement of the crack tip during the crack propagation phenomenon.

A 500 N force cell was used to measure the reaction force. The images of the two cameras, the reaction forces and the machine displacement were fully synchronized and registered at a frequency of 0.03 Hz. For each configuration, five samples were tested.

3.2. Experimental optimization of the ATDCB samples

For each value of the height h_{DCB} studied in the numerical preliminary work, tests were performed. For all values of h_{DCB}, the force-displacement curves presented good repeatability. The fracture surfaces were interfacial for h_{DCB} = 5 mm and h_{DCB} = 7.5 mm and were mixed for h_{DCB} = 10 mm. Because of the low values of h_{DCB}, a plasticization of the DCB substrate was observed. For each tested sample, the value of the residual bending was measured. The specimen with the 5 mm height had a mean residual bending of the DCB substrate of 37.0 mm and a bad repeatability when the 10 mm specimen had a better repeatability with a mean value of 7.3 mm. Finally, the specimen with the 7.5 mm height reached a mean residual bending of 17.8 mm.

Based on the experimental and numerical results exposed above, the criterion to choose the final specimen geometry for the ATDCB specimen were based on: i) the entire fracture surface, ii) the stable propagation on the DCB interface, iii) the less of plasticization of the DCB substrate, iv) a high mode ratio according to the previous VCCT calculations, and v) the best possible repeatability (curves and plasticization). According to the acceptance criterion, the 10 mm height was forsaken as they did not permit a fully interfacial fracture surface and the 5 mm height for the important plasticization and the discrepancy in the residual bending measured. Therefore, h = 7.5 mm fulfils at best all acceptance criteria previously described.

3.3. Interfacial unaged ATDCB

As it could be seen from the force-displacement curves in Figure 5**a**, the ATDCB test results presented good repeatability for the specimens at the unaged state. The force presented several plateaus until the end of the test; this was probably due to a step by step (stick-slip) crack propagation as pointed out in previous studies [35–37]. The compliance C was calculated by:

$$C = \frac{u}{F} \qquad \text{(Eq. 9)}$$

where u was the overall opening displacement and F was the reaction force along the loading axis.

The evolution of C as a function of the crack length a, plotted in Figure 5**b**, was not linear for the ATDCB specimen, contrary to results we should obtain with a TDCB normalized test. This nonlinear evolution was due to the low stiffness of the DCB upper substrate. Furthermore, the nonlinear evolution of the compliance could also be attributed to the change of the mode ratio with the crack growth highlighted previously and plotted for h_{DCB} = 7.5 mm. Last, the plasticization of the DCB upper substrate during the test will contribute also to the nonlinearity. Such discrepancies from the LEFM framework and the normalized tests configurations led the authors to develop numerical methods to deal with the evolution of the mode ratio and the plasticization of the substrates. The models developed and the calculation of the SERR will be presented in section 4.

3.4. Interfacial water aged ATDCB

The ATDCB specimens were aged for 4, 8, 12 and 16 months in deionized water bath at 40°C. Then they were tested under the same conditions as the ones at the unaged state, and the force-displacement curves are given in **Figure 6**. It could be noticed that all curves have the same shape as those issued for the unaged specimens given in Figure 5**a**, and present good repeatability. However, crack propagation started at a lower force value and the total displacement was much lower. This also affected the plasticization of the smaller substrate, which was significantly lower. The fracture surfaces were systematically interfacial (**Figure 7**). This was expected from the numerical calculations discussed before and also from the fact that water ageing mainly affects the interface failure properties with the substrates in adhesively bonded joints [38–40]. It can also be observed that the maximum load (**Figure 6**) was impacted by the water ageing effect.

4. Calculation of the interfacial SERR

In order to calculate the SERR at the interface between the adhesive and the upper substrate, an inverse identification methodology was built-up. In this method, FEM of the ATDCB test were developed to draw a numerical force-displacement curve. Then, an optimization of the SERR at the bi-material interface will be performed to fit the numerical response to the experimental results. Details of the FEM are given in this section.

4.1. Numerical model for ATDCB test

Building on the previous VCCT models previously presented, the Figure 2 shows the FE models used for the calculation of the interfacial *SERR* at the unaged state. Boundary conditions and material parameters were the same. For this model, in order to model failure at the interface between the upper substrate and the adhesive, the cohesive zone model (CZM) implementation of Abaqus® software was used. This implementation of the CZM theory with a linear failure law already gave interesting results in the understanding of bi-material interface failure in the study of composite materials [8]. In a first approximation, the failure stress identified of the adhesive material [24] was used as a failure parameter at the interface. The value of 29 MPa was used as critical value of a quadratic criterion defined by (Eq. 10 to predict the initiation of the interfacial crack. In (Eq. 10, *n*, *s* and *t* are the indices for the normal, the first shear and the second shear directions of the cohesive zone law.σ_i^0 with *i* equal to *n*, *s* or *t* define the maximum stress for the initiation of the crack.

Since the VCCT analysis, in the configuration of a DCB substrate thickness of h_{DCB} = 7.5 mm concluded on mode ratio calculated between 86% and 90%, the mode I is dominating all along the crack growth. So, it could be considered that only mode I failure could be modelled, and the damage variables of the cohesive zone could only be influenced by the mode I failure law.

So, an approximation of a failure only due to a pure tensile load could be done. Thus, σ_n^0 was considered equal to 29 MPa and the σ_t^0, σ_s^0 were set to high values in order to neglect effects of shear loadings: these hypotheses led to Eq. 11. A power-law was used for the energetic criterion defined by Eq. 12 where G_n, G_s and G_t are the energy release rate in mode I, mode II and mode III respectively. The *C* exponent relate to the critical energy release rate. The parameter $\alpha\alpha$ of the power law was considered equal to 1. Here, for the same reasons, only the mode I material parameter was considered, and G_s^C and G_t^C were set to high values (Eq.

13). The critical SERR in mode I, G_n was the parameter to identify by the inverse identification process built-up.

$$\left\{\frac{\langle\sigma_n\rangle}{\sigma_n^0}\right\}^2+\left\{\frac{\sigma_s}{\sigma_s^0}\right\}^2+\left\{\frac{\sigma_t}{\sigma_t^0}\right\}^2=1 \quad \text{(Eq. 10)}$$

$$\left\{\frac{\langle\sigma_n\rangle}{\sigma_n^0}\right\}^2=1 \quad \text{(Eq. 11)}$$

$$\left\{\frac{G_n}{G_n^C}\right\}^\alpha+\left\{\frac{G_s}{G_s^C}\right\}^\alpha+\left\{\frac{G_t}{\sigma_t^C}\right\}^\alpha=1 \quad \text{(Eq. 12)}$$

$$\left\{\frac{G_n}{G_n^C}\right\}=1 \quad \text{(Eq. 13)}$$

Two FEM were built up: the first case considered all materials elastics (named "Elastic model") and the second case considered an elastic behaviour for the adhesive joint and the identified elastic-plastic behaviour for the substrates (named "Elastic-plastic model"). Choice of the model and the material parameters for the substrate material are defined in the next section.

4.2. Elastic-plastic behaviour for metallic substrates

Since significant plasticization of DCB substrates occurred, it was necessary to take the plastic mechanical behaviour of the substrates into account. To do so, the behaviour was characterized by performing load-unload tests. These tests were performed on tension-compression loading on dog-bone specimens which a cross section of 5 x 15 mm² and useful length of 30 mm. The specimens were extracted of the same metallic sheet of 5 mm than the ATDCB substrates. The characterization tests followed the methodology proposed by Levieil *et al.* [41] and allowed identifying the different types of hardening and their amplitude (**Figure 8**). In order to describe accurately the substrate behaviour involving stress and unstressed parts during the crack propagation a model, including two isotropic hardenings (R) and three kinematic hardenings ($\underline{\underline{X}}_i$), was used. The comparison between the experimental response and the model result are plotted in **Figure 8**. For confidentiality matter, stresses are normalized by the yield strength of the material σ_y and strains by $\varepsilon_y = \sigma_y/E$. For true strains

inferior to 0.5 %, the isotropic hardening was negative. In fact, these metallic sheets were produced by cold rolling which could induce hardening during the process. The metallic material was not really under the scope of this study, so the authors beg the reader to accept the good identification of the mechanical behaviour. The identified behaviour and the substrates material parameters, summarized in Table 2, will be integrated in the FE numerical simulations. For confidentiality matters, parameters (C_1, C_2, C_3) and (Q_1, Q_2) are divided by the yield strength σ_y.

4.3. Identification of the critical SERR G_I^C

The critical SERR in mode I, G_I^C was the parameter to identify, in the inverse process, using the force-displacement numerical response and experimental results mean curve (Figure 10). The optimization was performed with the function to minimize (Eq. 14):

$$\sum \left(F_{\exp} - F_{num} \right)^2 < p \qquad \text{(Eq. 14)}$$

where, $F_{\exp}$ is the experimental load, F_{num} is the numerical load and p is the wished accuracy.

The results, given in Table 3 for each water ageing period and each model, were obtained considering a convergence p value of 10^{-2}. Numerical minimization between the model response and experimental results was only based on a part of the force-displacement curve. Indeed, in order to avoid the effect of crack initiation, the crack propagation corresponding to 50-85% of the opening displacement at failure was only considered. At unaged state, Figure 9 shows the results after the optimisation process of the G_I^C parameter, from the elastic and elastic-plastic models: a good correlation is obtained in particular when examining compliance vs. crack length (Figure 9**b**). The unaged state is particular by the quite high plasticization of the upper substrate. All other ageing periods led to low numerical plasticization. Figure 10 shows the results for several ageing periods. The tensile strength of the adhesive was introduced in the CZM law. This strength was identified using adhesive material bulk samples. However, the characterization of the interfacial tensile strength should help to further improve the numerical predictions. This objective will lead to further works.

As it has been shown in [23], the mechanical behaviour of the adhesive considerably influences its values of the SERR. The fracture curves in **Figure 6** show that the maximum force increased after 4 months of water ageing. This phenomenon could be explained by the change

of the adhesive behaviour, since it is well known that water ageing also contribute to plasticize the adhesive [38,42]. Nonetheless, the results for the SERR were analysed here by means of the LEFM theory. **Figure 11** shows the evolution of the SERR regarding to the ageing time for the adhesive fracture. At the unaged state, the energy of the plasticization of the substrates needs to be removed in order to estimate the adhesive SERR. For all ageing periods, the residual bending measured for each ATDCB sample is given in Table 4.

5. Conclusions and discussions

The main purpose of this study was to determine the Strain Energy Release Rate (SERR) considering an interfacial crack propagation (interfacial failure) for a metallic material assembly with an epoxy-based adhesive. Therefore, the authors proposed in this paper an experimental way to propagate a crack adhesively and a methodology to determine for mode I dominated failure the SERR G_I^C. This methodology was extended to the study of the effect of water ageing.

In a preliminary study, different heights of t substrates were tested in an ATDCB configuration in order to optimize an interfacial failure and to be as close as possible to the LEFM framework. Using 7.5 mm substrates, the crack propagates adhesively and stably now. A good repeatability of the tests was observed for the unaged state and the experiments were reproduced for 4, 8, 12 and 16 months of immersion in 40°C deionised water with also repeatable results. All results were compared in terms of force-displacement curves, compliance function of the crack length and finally by the SERR. Nevertheless, during ATDCB tests, substrates plasticized. So, it was necessary to take into account the energy of the metallic material plasticization in the measurement of the SERR calculated. Therefore, using FEM and the CZM theory, an inverse identification is proposed to determine G_I^C considering the non-linear behaviour of the metallic substrates. On unaged samples, a SERR G_I^C=¿2.5 N/mm was estimated in mode I. This value, after 4 months of water ageing, dropped to a G_I^C=¿0.6 N/mm. But after 8 months, it grew slightly to 0.8 N/mm and until 1.2 N/mm at 16 months. This non-monotonic evolution could be due to the influence of the water uptake of the adhesive joint. The mechanical behaviour of the adhesive and its own plasticization energy may have an influence on the energy released during the test. The adhesive mechanical behaviour evolves with the ageing changing and its influence may change the evolution of G_I^C

with the water ageing. A demonstration of this phenomenon with respect to water uptake can be found in previous studies [38,43–45]. In future works including the effect of water uptake in the FEM, evolution the adhesive mechanical behaviour could be taken into account. To do so, the first step will be to resolve the problem of the CZM with non-linear materials, the second will be to add the numerical water diffusion, and finally the objective will be to propose a numerical way to take all material behaviours (linear and non-linear) with the evolution of the adhesive material parameter with the water ageing.

Pursuing the objective of a model integrating the competition between interfacial failure and cohesive failure (in the adhesive joint) a comparison could be performed between the interfacial SERR and the cohesive SERR. A previous work leaded the authors to evaluate, with the use of LEFM a G_I^C for the same adhesive [24]. Nevertheless, comparison of SERR is not sufficient for an overall approach of failure. Indeed, the tensile strength at the interface may play an important role in failure. As a first approximation, in the CZM implementation at the interfaces, a cohesive value was used to model initiation. This strength may be different at the interface and should lead to an experimental campaign to identify it.

6. Acknowledgements

This study is part of the INDUSCOL project, and the authors wish to associate the industrial partner of this project: Naval Group. This work benefited from France Energies Marines in France and State financing managed by the National Research Agency under the Investments for the Future program bearing the reference ANR-10-IED-0006-08.

References

1 IRENA. *Renewable Energy Statistics 2019*. IRENA; 2019.

2 REN21. *Renewables 2019 Global Status Report*. France: REN21 Secretariat: Paris; 2019.

3 Brøndsted P, Lilholt H, Lystrup A. Composite materials for wind power turbine blades. *Annu Rev Mater Res*. 2005;35: 505–538.

4 Davies P, Germain G, Gaurier B, Boisseau A, Perreux D. Evaluation of the durability of composite tidal turbine blades. *Philos Trans R Soc Math Phys Eng Sci*. 2013;371: 20120187.

5 Desjardins D, Oltra R, eds. *Corrosion sous contrainte: phénoménologie et mécanismes : [Ecole d'automne], Bombannes 1990, [23 au 28 septembre*. Les Ulis (France): Editions de physique; 1992.

6 Leguillon D. Strength or toughness? A criterion for crack onset at a notch. *Eur J Mech - ASolids*. 2002;21: 61–72.

7 Carrere N, Martin E, Leguillon D. Comparison between models based on a coupled criterion for the prediction of the failure of adhesively bonded joints. *Eng Fract Mech*. 2015;138: 185–201.

8 Camanho P, Dávila C. *Mixed-Mode Decohesion Finite Elements for the Simulation of Delamination in Composite Materials*. NASA; 2002.

9 Griffith AA, Taylor GI. VI. The phenomena of rupture and flow in solids. *Philos Trans R Soc Lond Ser Contain Pap Math Phys Character*. 1921;221: 163–198.

10 Ripling E, Mostovoy S, Patrick R. Application of Fracture Mechanics to Adhesive Joints. *Adhesion*. January 1964.

11 Chang MD, Devries KL, Williams ML. The Effects of Plasticity in Adhesive Fracture. *J Adhes*. 1972;4: 221–231.

12 Begley JA, Landes JD. The J Integral as a Fracture Criterion. *ASTM*. 1972.

13 Wells AA. Fracture control: Past, present and future. *Exp Mech*. 1973;13: 401–410.

14 DeVries KL, Williams ML, Chang MD. Adhesive fracture of a lap shear joint. *Exp Mech*. 1974;14: 89–97.

15 Mulville DR, Mast PW, Vaishnav RN. Strain energy release rate for interfacial cracks between dissimilar media. *Eng Fract Mech*. 1976;8: 555–565.

16 ASTM D6671 / D6671M-19. *Standard Test Method for Mixed Mode I-Mode II Interlaminar Fracture Toughness of Unidirectional Fiber Reinforced Polymer Matrix Composites*. West Conshohocken: ASTM International; 2019.

17 ASTM D3433 - 99. *ASTM D3433 - 99 : Standard Test Method for Fracture Strength in Cleavage of Adhesives in Bonded Metal Joints*. ASTM International; 2012.

18 ISO 25217. *ISO 25217 : Adhesives - Determination of the Mode 1 Adhesive Fracture Energy of Structural Adhesive Joints Using Double Cantilever Beam and Tapered Double Cantilever Beam Specimens*. International Organization for Standardization; 2009.

19 ASTM D7905/7905M-14. *Test Method for Determination of the Mode II Interlaminar Fracture Toughness of Unidirectional Fiber-Reinforced Polymer Matrix Composites*. ASTM International

20 ISO 15114:2014. *Fibre-Reinforced Plastic Composites — Determination of the Mode II Fracture Resistance for Unidirectionally Reinforced Materials Using the Calibrated End-Loaded Split (C-ELS) Test and an Effective Crack Length Approach*. International Organization for Standardization; 2014.

21 Brito CBG, Sales RCM, Donadon MV. Effects of temperature and moisture on the fracture behaviour of composite adhesive joints. *Int J Adhes Adhes*. 2020;100: 102607.

22 Hutchinson JW, Suo Z. Mixed Mode Cracking in Layered Materials. In: Hutchinson JW, Wu TY, eds. *Advances in Applied Mechanics*. Vol 29. Elsevier; 1991:63–191.

23 Stamoulis G, Carrere N. Linear elastic analysis of the loading rate dependency of the fracture properties of structural adhesives in the mixed mode I+II plane. *Eng Fract Mech*. 2020;225: 106840.

24 Leplat J, Stamoulis G, Bidaud P, Thévenet D. Investigation of the mode I fracture properties of adhesively bonded joints after water ageing. *J Adhes*. 2020;0: 1–22.

25 Cognard JY. Numerical analysis of edge effects in adhesively-bonded assemblies application to the determination of the adhesive behaviour. *Comput Struct*. 2008;86: 1704–1717.

26 Silva LFM da, Esteves VHC, Chaves FJP. Fracture toughness of a structural adhesive under mixed mode loadings. *Mater Werkst*. 2011;42: 460–470.

27 Park S, Dillard DA. Development of a simple mixed-mode fracture test and the resulting fracture energy envelope for an adhesive bond. *Int J Fract*. 2007;148: 261–271.

28 Nunes FAA, Campilho RDSG. Mixed-mode fracture analysis of adhesively-bonded joints using the ATDCB test specimen. *Int J Adhes Adhes*. 2018;85: 58–68.

29 Bennati S, Colleluori M, Corigliano D, Valvo PS. An enhanced beam-theory model of the asymmetric double cantilever beam (ADCB) test for composite laminates. *Compos Sci Technol*. 2009;69: 1735–1745.

30 Shokrieh MM, Zeinedini A. A Novel Method for Calculation of Strain Energy Release Rate of Asymmetric Double Cantilever Laminated Composite Beams. *Appl Compos Mater*. 2014;21: 399–415.

31 Campilho RDSG, Banea MD, Chaves FJP, Silva LFM da. eXtended Finite Element Method for fracture characterization of adhesive joints in pure mode I. *Comput Mater Sci*. 2011;50: 1543–1549.

32 Sukumar N, Prévost J-H. Modeling quasi-static crack growth with the extended finite element method Part I: Computer implementation. *Int J Solids Struct*. 2003;40: 7513–7537.

33 ISO 527. *ISO 527 : Plastics - Determination of Tensile Properties*. International Organization for Standardization; 2012.

34 Krueger R. Virtual crack closure technique: History, approach, and applications. *Appl Mech Rev*. 2004;57: 109–143.

35 Tsai K-H, Kim K-S. Stick-slip in the thin film peel test—I. the 90° peel test. *Int J Solids Struct*. 1993;30: 1789–1806.

36 Wu-Bavouzet F, Clain-Burckbuchler J, Buguin A, Gennes† P-GD, Brochard-Wyart F. Stick-Slip: Wet Versus Dry. *J Adhes*. 2007;83: 761–784.

37 Viswanathan K, Sundaram NK. Distinct stick-slip modes in adhesive polymer interfaces. *Wear*. 2017;376–377: 1271–1278.

38 Bordes M, Davies P, Cognard J-Y, Sohier L, Sauvant-Moynot V, Galy J. Prediction of long term strength of adhesively bonded steel/epoxy joints in sea water. *Int J Adhes Adhes*. 2009;29: 595–608.

39 Ashcroft IA, Comyn J. Effect of Water and Mechanical Stress on Durability. In: da Silva LFM, Öchsner A, Adams RD, eds. *Handbook of Adhesion Technology*. Berlin, Heidelberg: Springer; 2011:787–822.

40 Calvez P, Bistac S, Brogly M, Richard J, Verchère D. Mechanisms of Interfacial Degradation of Epoxy Adhesive/Galvanized Steel Assemblies: Relevance to Durability. *J Adhes*. 2012;88: 145–170.

41 Levieil B, Doudard C, Thevenet D, Bridier F, Ezanno A, Calloch S. An original simplified method based on the use of an adjustable localization operator for low-cycle fatigue life predictions in the case of confined plasticity. *Theor Appl Fract Mech*. 2019;104: 102383.

42 Ilioni A, Badulescu C, Carrere N, Davies P, Thévenet D. A viscoelastic-viscoplastic model to describe creep and strain rate effects on the mechanical behaviour of adhesively-bonded assemblies. *Int J Adhes Adhes*. 2018;82: 184–195.

43 Tual N. Durabilité des composites carbone/époxy pour applications pales d'hydroliennes. November 2015.

44 Ilioni A, Gac P-YL, Badulescu C, Thévenet D, Davies P. Prediction of Mechanical Behaviour of a Bulk Epoxy Adhesive in a Marine Environment. *J Adhes*. 2019;95: 64–84.

45 Rudawska A, Abdel Wahab M, Müller M. Effect of ageing process on mechanical properties of adhesive tubular butt joints in aqueous environment. *Int J Adhes Adhes*. 2020;96: 102466.

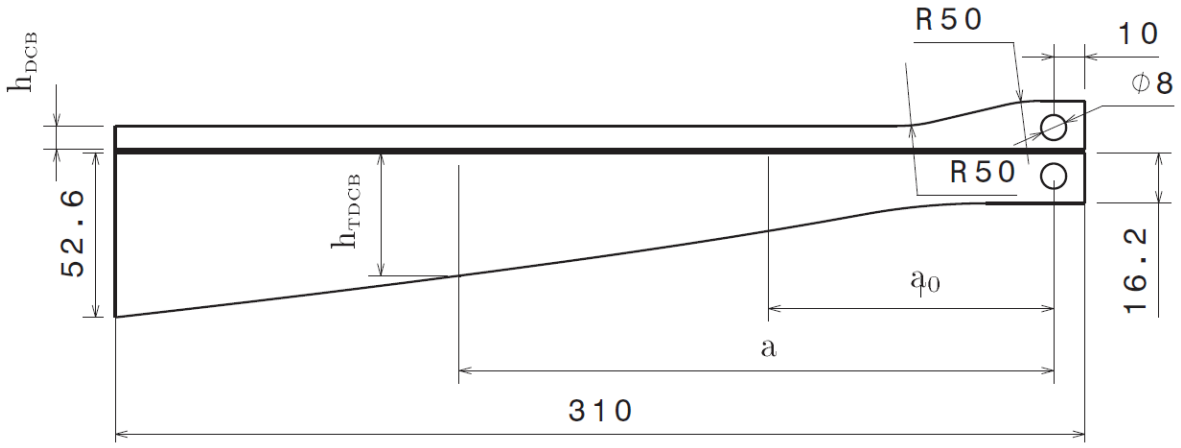
R50
10
ϕ8
R50
h_{DCB}
52.6
h_{TDCB}
a_0
16.2
a
310

Figure 1: Dimensions of the ATDCB specimen (mm)

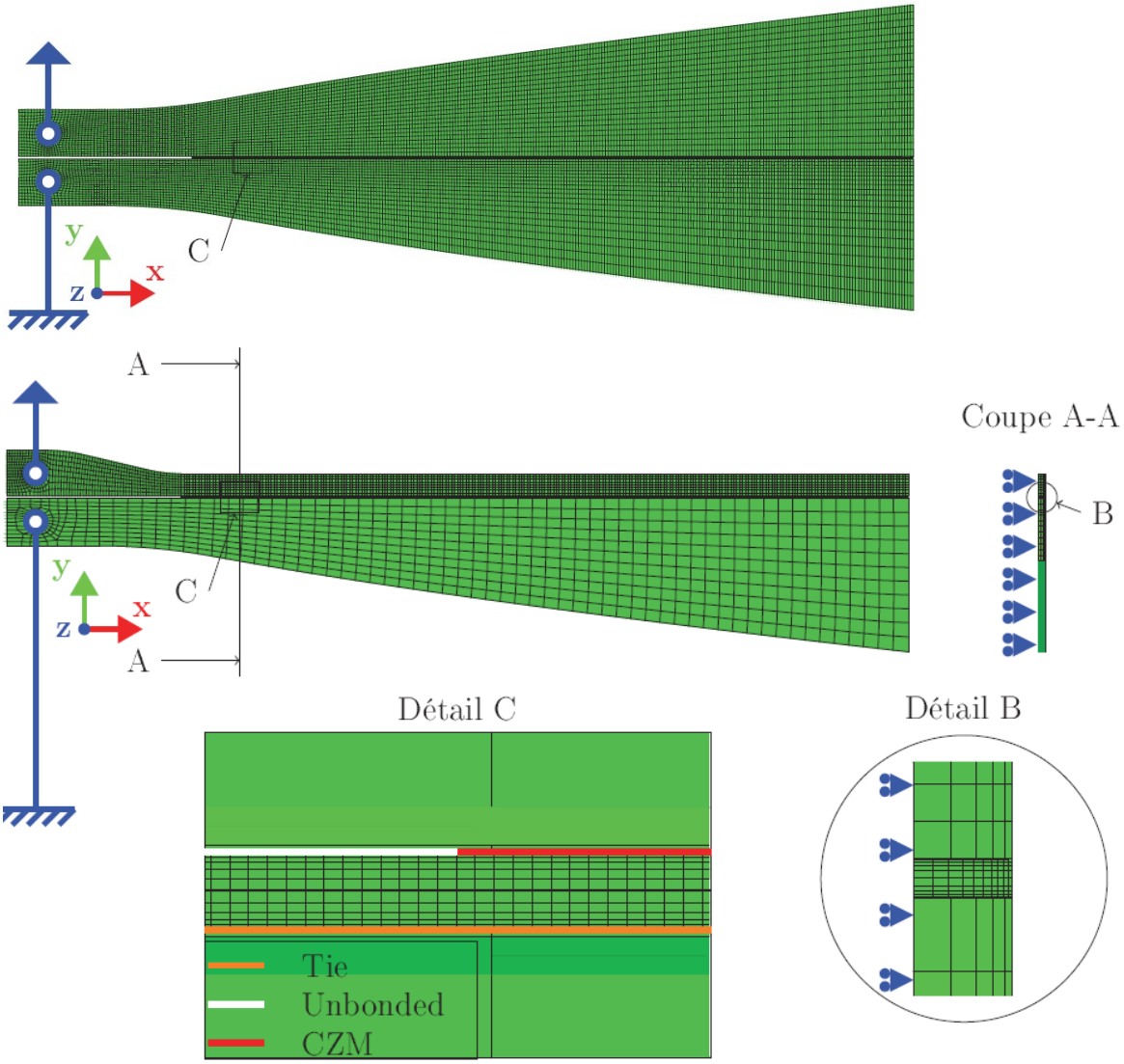

Figure 2: Finite element model of the TDCB and ATDCB specimen

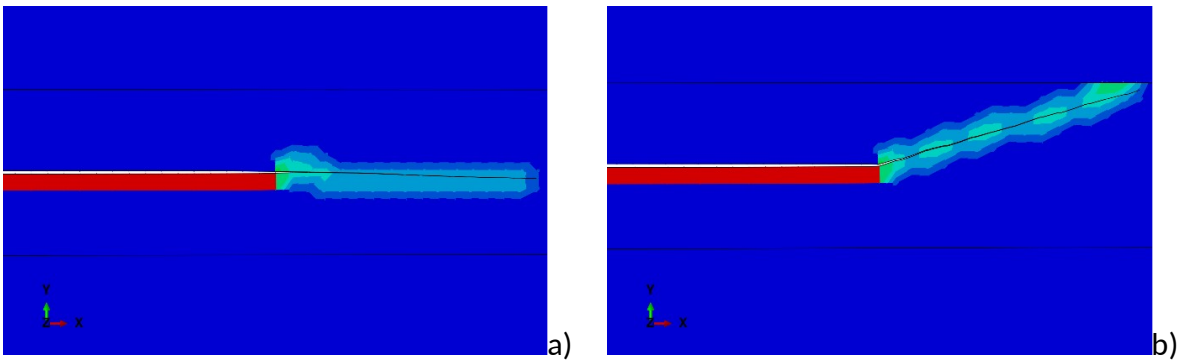

Figure 3: XFEM results of crack propagation for TDCB specimen (a) for ATDCB specimens with h_{DCB}: 7.5 mm (b)

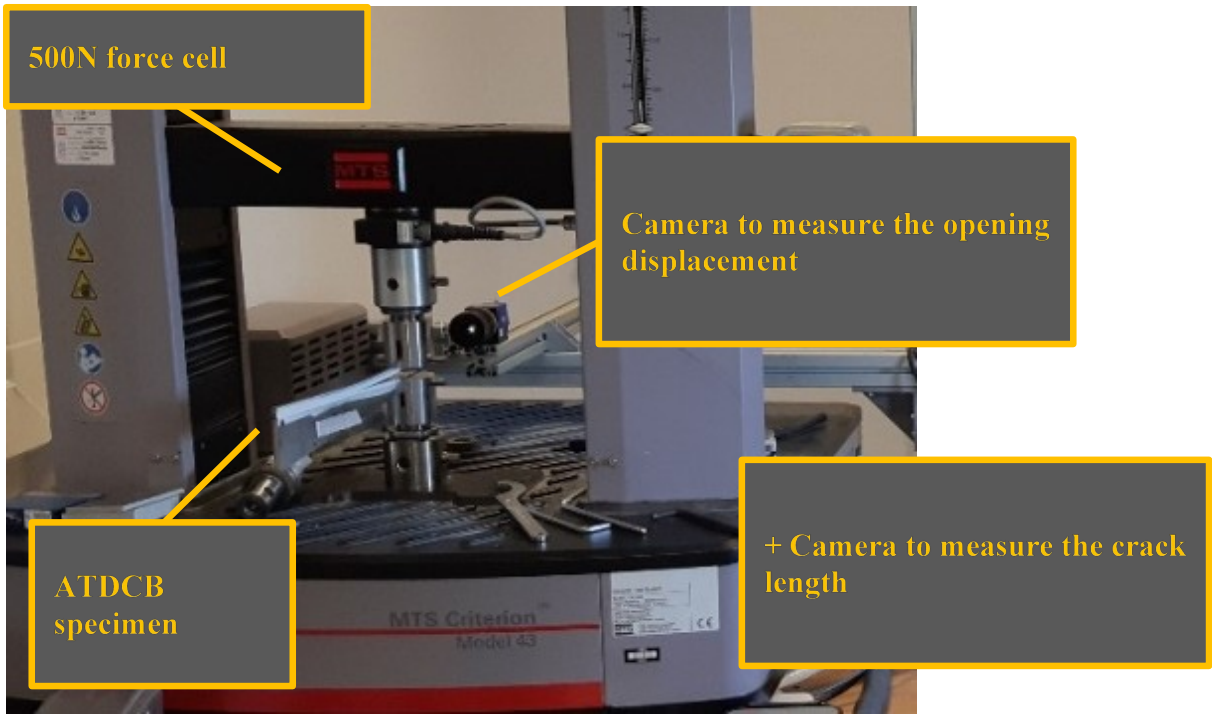

Figure 4: Experimental setup

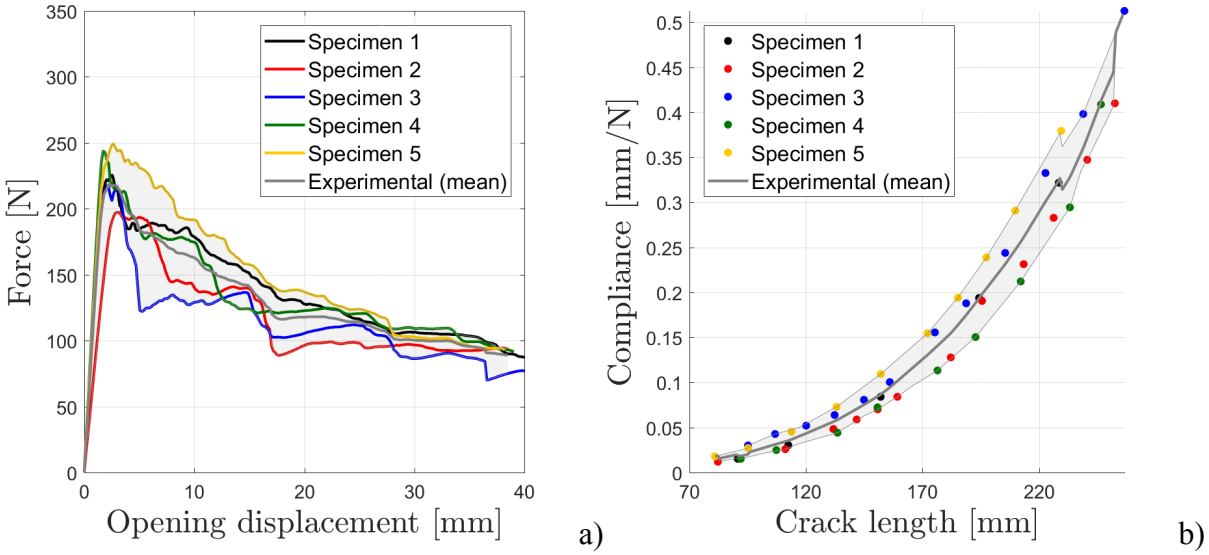

Figure 5: ATDCB specimens (unaged state): force vs. opening displacement (a) and compliance vs. crack length (b)

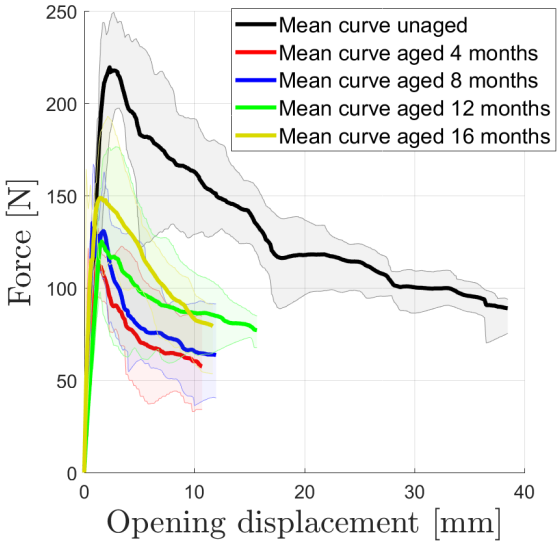

Figure 6: Mean force-displacement curve of each water ageing period

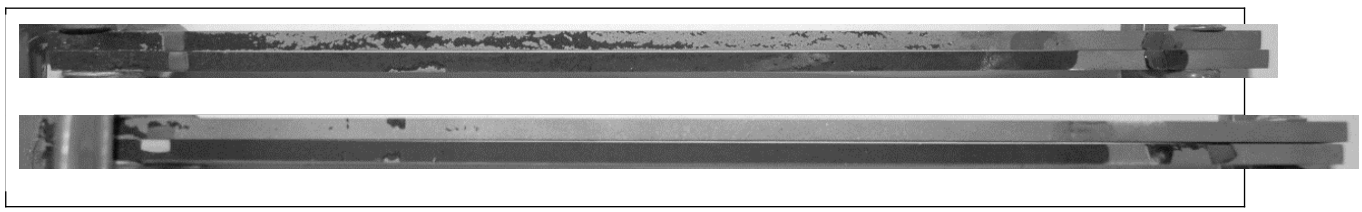

Figure 7: Fracture surfaces of ATDCB specimens: unaged (a) and 16 months water ageing (b)

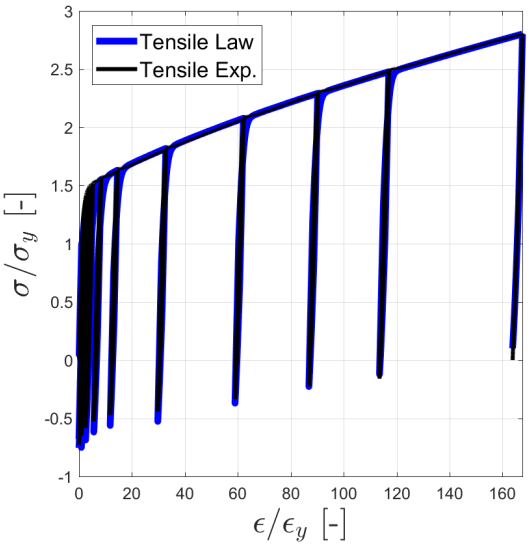

Figure 8: Load-unload test (metallic material)

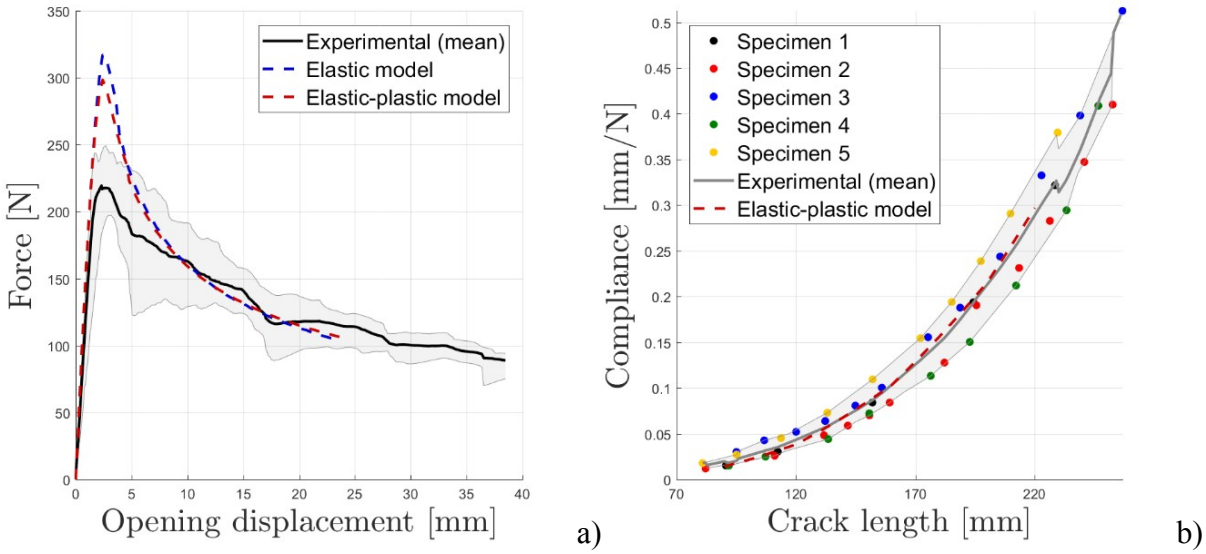

Figure 9: Experimental results (mean) and numerical predictions: force *vs.* displacement (a) and compliance *vs.* crack length (b) at unaged state

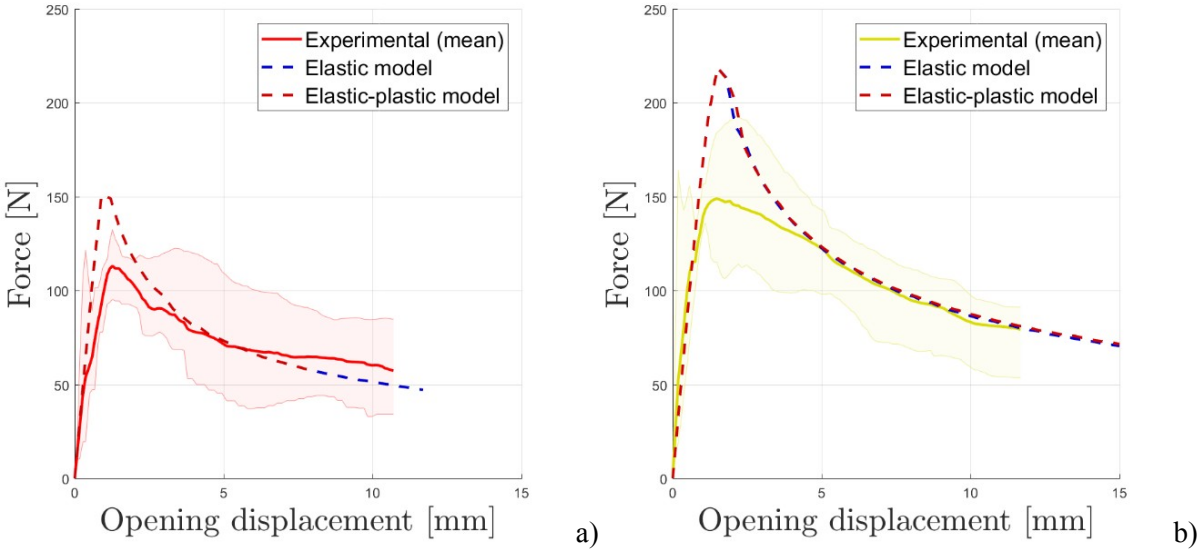

Figure 10: Experimental (mean) and numerical force-displacement curves for the identification of the interfacial G_{IC}: 4 months (a) and 16 months (b) water ageing

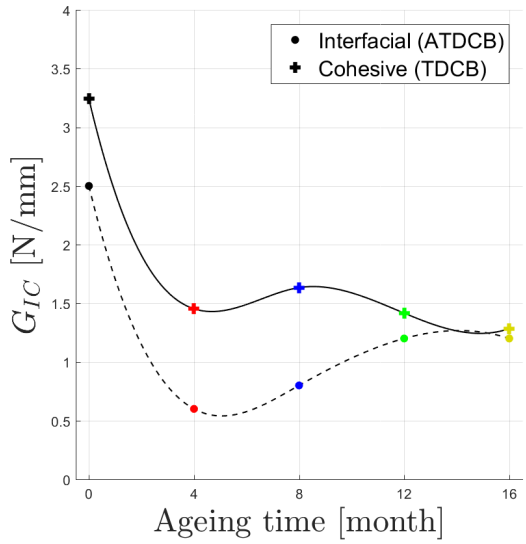

Figure 11: SERR of the ageing time calculated by LEFM

Parameter	ν	E (MPa)	$\square_n^0$ (MPa)	G_I^c (N/mm)
Value	0.4	1 550	29	3.2

Table 1: Material properties at unaged state (adhesive material)[24]

Parameter	ν	C_1/σ_y	γ_1	C_2/σ_y	C_3/σ_y	γ_3	b_1	Q_1/σ_y	b_2	Q_2/σ_y
Value	0.3	673.68	800	3.61	3.16	10	2000	-0.37	10	0.10

Table 2: Material properties (metallic material)

G_I^C [N/mm]	Elastic model	Elastic-plastic model
Unaged	2.70	2.50
4 months	0.60	0.60
8 months	0.80	0.80
12 months	1.20	1.20
16 months	1.20	1.20

Table 3: Results of the critical strain energy release rate (mode I)

Ageing Time [month]	0	4	8	12	16
Residual bending [mm]					
Sample 1	22	3	3	7	4
Sample 2	17	3	6	6	5
Sample 3	17	4	4	5	6
Sample 4	19	3	2	5	4
Sample 5	18	4	6	7	5
Sample 6	-	-	-	-	6
Sample 7	-	-	-	-	6
Sample 8	-	-	-	-	5
Mean	17.8	3.4	4.2	6.0	4.8
Standard deviation	1.0	0.5	1.8	1.0	0.8

Table 4: Residual bending of all tested ATDCB samples (unaged and aged states)